ELSEVIER

Ultrathin FeTe nanosheets with tetragonal and hexagonal phases synthesized by chemical vapor deposition

Xingguo Wang [1], Ce Bian [2], Yixiang He [1], Jie Guo [1], Peng Zhang [1,*], Lixuan Liu [1], Yi Wei [3], Lingjia Meng [1], Huaning Jiang [1], Bixuan Li [1], Anmin Nie [4,*], Lihong Bao [2,5,*], Yongji Gong [6,*]

[1] School of Materials Science and Engineering, Beihang University, Beijing 100191, PR China
[2] Institute of Physics & University of Chinese Academy of Sciences, Chinese Academy of Sciences, Beijing 100190, PR China
[3] State Key Laboratory of Organic-Inorganic Composites, Beijing Key Laboratory of Electrochemical Process and Technology for Materials, Beijing University of Chemical Technology, Beijing 100029, PR China
[4] Center for High Pressure Science, State Key Laboratory of Metastable Materials Science and Technology, Yanshan University, Qinhuangdao 066004, PR China
[5] Songshan Lake Materials Laboratory, Dongguan, Guangdong 523803, PR China
[6] Center for Micro-Nano Innovation of Beihang University, Beijing 100191, PR China

2D functional materials, such as 2D magnet and superconductor, spark massive interests from synthesis, manipulation to application. Especially, $FeTe_x$ with multi-phases provides an ideal platform to explore the possible superconducting, ferromagnetic or antiferromagnetic properties and even their functional heterostructures. Herein, we report a facile chemical vapor deposition (CVD) approach to synthesize ultrathin tetragonal FeTe (down to monolayer), hexagonal FeTe (down to 2.3 nm), and Fe-rich hexagonal FeTe with superlattice by tuning the growth temperature according to the phase diagram. Scanning transmission electron microscopy (STEM) is further performed to confirm the difference among these various FeTe phases. Magneto-transport illustrates that the tetragonal device displays a high linear magnetoresistance (LMR) up to 10.5% at 1.9 K, and the LMR of hexagonal FeTe reaches 5.8% at 1.9 K. Interestingly, O doped tetragonal thick FeTe displays a superconducting transition at 9 K, which can persist even at 16 T. In summary, this study illustrates a phase-selective synthesis of $FeTe_x$ ultrathin crystals, providing promising opportunities to construct complicated devices such as ferromagnet/antiferromagnet, magnet/superconductor heterostructures.

Introduction

Two-dimensional (2D) materials especially functional 2D layered materials, such as superconductors [1,2], 2D magnets [3–5], topological insulators [6], ferroelectric materials [7], and photoluminescence materials [8], have attracted increasing attention because of their promising applications in memory, sensor, electronics, and optoelectronics [9–12]. Among them, 2D superconductors have attracted intensive attention as well recently. For instance, bilayer graphene with magic angles [1], exfoliated ZrNCl nanosheets [13], HfNCl [14], 2H-NbS_2 [15–17], MoS_2 [18], $Bi_2Sr_2CaCu_2O_{8+\delta}$ [2], layered Fe-based superconductor [19–21], etc. have been reported to be superconductors with various transition temperatures, which may provide good platforms to design new devices and study the superconducting mechanism. However, most of the reported 2D superconductors are fabricated by mechanical exfoliation or MBE. Facial and controllable preparation of such a 2D superconductor still poses a challenge. To our best knowledge, only a few 2D superconductors, such as $NbSe_2$ [15], Mo_2C [22], etc., can be synthesized by the convenient

* Corresponding authors.
E-mail addresses: Zhang, P. (x_l_zhang@buaa.edu.cn), Nie, A. (anmin@ysu.edu.cn), Bao, L. (lhbao@iphy.ac.cn), Gong, Y. (yongjigong@buaa.edu.cn).

 https://doi.org/10.1016/j.mattod.2020.11.022

CVD method. Hence, exploring more 2D superconducting systems and developing a simple method to synthesize those 2D superconductors seem to be necessary. Furthermore, the study of superconducting behavior on the scale of 2D materials can undoubtedly deepen the understanding of superconductivity, further exploring the mechanism behind. Besides, 2D materials with long-range magnetic order also attract substantial interest ranging between methods to synthesize magnetic 2D crystals [23–29], ways to adjust magnetic properties [30–33], and novel device design to realize multifunctional applications. Nowadays, some 2D transition metal chalcogenides with magnetic elements such as Cr, Mn, Fe, V are predicated to be ferromagnetic or antiferromagnetic [34–37]. Nevertheless, these 2D systems can usually form into multiphase crystals with a distinct composition according to the corresponding phase diagrams, which undoubtedly brings non-trivial challenges to explore their properties on the scale of atomic thickness experimentally.

Among them, iron and tellurium can react to form various $FeTe_x$ phases at different temperature ranges, where x varies from 1 to 2 [38–39]. On the one hand, the typical layered tetragonal FeTe phase indicates antiferromagnetic behavior with the Neel temperature ~70 K [40]. Notably, the antiferromagnetic properties in tetragonal FeTe can be inhibited by O, S, or Se doping, and the doped FeTe crystals can probably transfer into superconductors, which attracted numerous study [41–44]. On the other hand, another FeTe phase demonstrates hexagonal symmetry, which exhibits a NiAs type crystal structure [45]. Recently, Liu et. al reported CVD-growth of hexaonal FeTe and ferromagnetism was observed in the hexagonal FeTe nanosheets [46]. Besides the hexagonal and tetragonal FeTe phases, there are $FeTe_2$ and some non-integer stoichiometric phases as well, providing the possibilities to get different magnetic properties in this system [47]. In this case, the phase-selective growth of $FeTe_x$ is highly desired to be realized and then to study their magnetic, electric properties, and even the relationship between them. Furthermore, utilizing these 2D platforms, multifunctional electronis and spintronics can be put into practice in a certain situation.

Herein, we report a facile CVD approach to selectively synthesize tetragonal FeTe, hexagonal FeTe and Fe-rich hexagonal FeTe with superlattice crystals by tuning the growth temperatures according to the phase diagram [38]. The thickness of the nanosheets of each phase on SiO_2/Si substrates can be efficiently adjusted by the growth time and the thickness of the layered tetragonal phase can be tuned down to monolayer. Optical microscopy (OM) images illustrate that the tetragonal crystals display a square shape while hexagonal FeTe crystals are trigonal or hexagonal with the lateral domain size ranging from several to tens of microns. The smallest thickness of tetragonal obtained is 0.9 nm probed by Atomic force microscopy (AFM), together with the nonlayered hexagonal FeTe crystals showing the minimum thickness of 2.3 nm. Additionally, Raman and X-ray photoemission spectroscopy (XPS) is further carried out to compare and analyze the vibration modes and chemical states of these two kinds of FeTe crystals. The detailed crystal structure and high crystalline quality are confirmed by aberration-corrected scanning transmission electron microscopy-annular dark field (STEM-ADF) imagings, which indicate a typical P4/nmm structure of the tetragonal FeTe and two different chemical compositions and crystal structures of the hexagonal FeTe. Interestingly, the normal hexagon shows a NiAs type crystal structure with the chemical stoichiometric ratio of 1:1 and the other Fe-rich hexagonal FeTe crystals illustrate a superlattice structure. Magneto-transport studies are further conducted to explore the properties of tetragonal and normal hexagonal FeTe nanosheets. Both two kinds of FeTe illustrate considerable temperature-dependence linear magnetoresistance (LMR) with the magnetic field, among which 10.5% LMR for tetragonal FeTe while 5.8% for hexagonal FeTe are achieved. Notably, a superconducting transition at 9 K is observed in O doped tetragonal FeTe nanosheets, where the O concentration is probed by Auger Electron spectrum. Above all, this work illustrates a controllable way to selectively synthesize FeTe crystals with various phases, which may provide a promising opportunity to study the properties of ultrathin $FeTe_x$ nanosheets with various thicknesses and to build up ferromagnet/antiferromagnet and superconductor/magnet heterostructures.

Results and discussion

Effect of temperature on phase selection

According to the iron-tellurium phase diagram in Fig. S1, iron and tellurium can form into multiple phases, which undoubtedly increases the difficulty to selectively synthesize a certain Fe-Te crystal with desired composition and structures. However, hexagonal and tetragonal FeTe show high sensitivity with the growth temperature. Hence, phase-controllable synthesis of FeTe crystals may be achieved by adjusting the growth temperature. Fig. 1a illustrates the growth mechanism of tetragonal and hexagonal FeTe crystals, in which tellurium powder and iron (II) chloride powder are used as precursors placed upstream of the quartz tube respectively. 50 sccm Ar/H_2 mixed gas is used as the carrier gas to increase the reactivity in the CVD process. Nonlayered hexagonal FeTe crystals can be obtained at high temperature while layered tetragonal FeTe nanosheets can be synthesized at low temperature, which may be caused by the better thermodynamic stability of hexagonal FeTe than that of tetragonal one at high temperature. More details are shown in the Methods.

Fig. 1b-e clearly shows the evolution of the hexagonal/tetragonal FeTe ratio with the synthesis temperature. The resulting nanoplates obtained at lower temperatures ranging from 600 to 680 °C mainly display rectangular or square shapes. When the temperature is adjusted between 680–710 °C, the as-grown FeTe nanoplates exhibit a mixed morphology with both square and hexagonal or triangular shapes. Furthermore, when the growth temperature is increased over 710 °C, the hexagonal FeTe nanoplates play a predominant role. Fig. 1b-e indicates the typical OM images obtained at 630, 690 and 740 °C respectively.

Effect of deposition time on the thickness

Even though growth temperature has a certain influence on the thickness of the resulting nanosheets, the deposition time still plays an important role. Hence, to obtain FeTe nanosheets with various thicknesses, deposition time is carefully tuned. Fig. 1f-h shows the OM images of the thinnest tetragonal FeTe crystals synthesized with deposition time 2, 4, 8 min respectively, among which the smallest height of the obtained tetragonal FeTe is

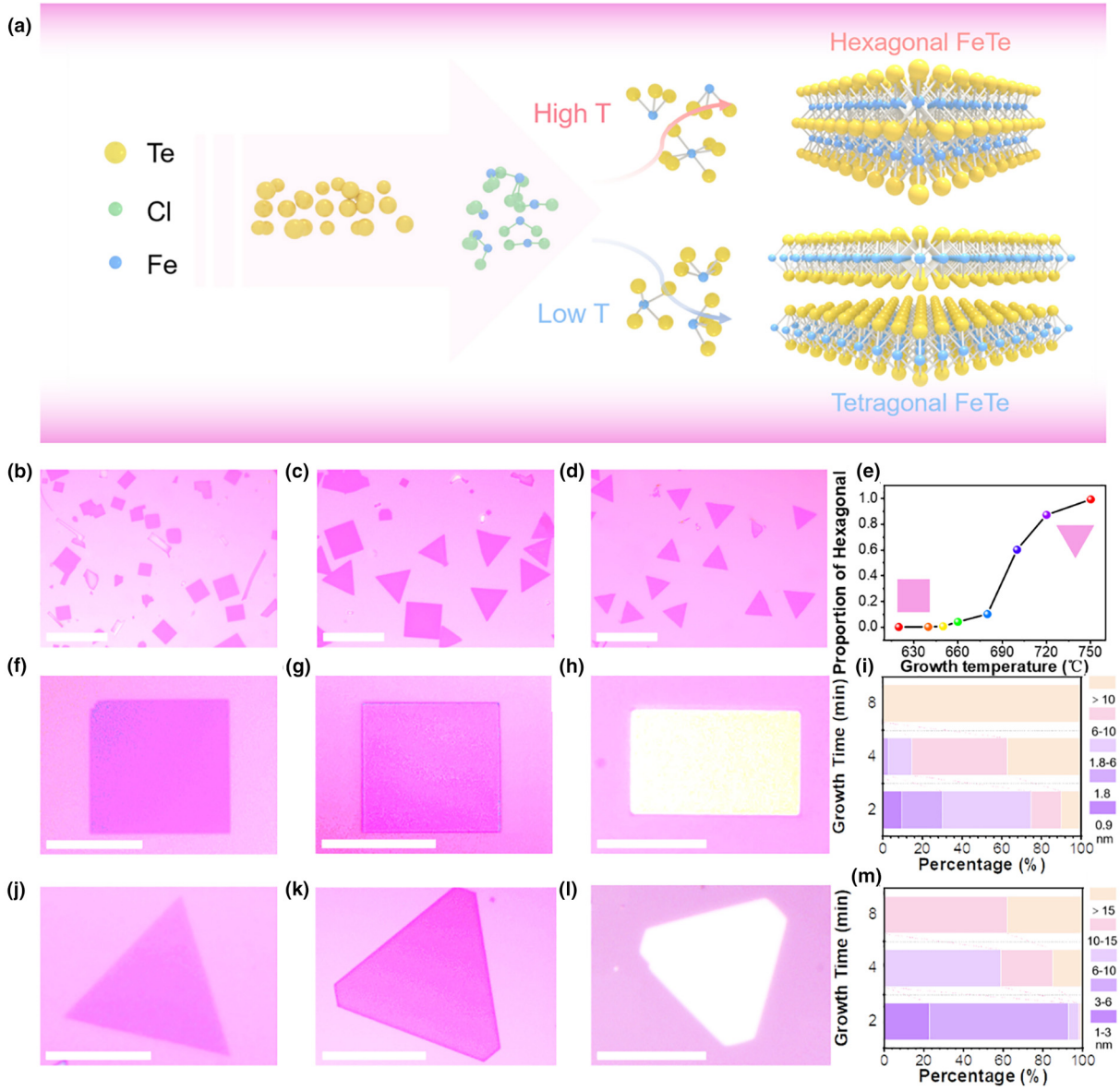

FIGURE 1

Growth mechanism and morphology of tetragonal and hexagonal FeTe crystals. (a) The schematic illustration of the preparation process. Tellurium powder is placed upstream of the quartz tube and $FeCl_2$ is used as Fe precursor downstream. The phase and shape of the as-synthesized FeTe nanoplates can be efficiently tuned by temperature. Yellow, blue and green balls represent Te, Fe and Cl atoms respectively. (b–d) Optical microscopy (OM) images of ultrathin FeTe nanoplates with a distinguished shape on SiO_2/Si obtained at 630, 690 and 740 °C respectively. (e) The evolution of the hexagonal/tetragonal FeTe ratio with the synthesis temperature. (f–h) OM images of tetragonal FeTe crystals with different color contrast indicating various thickness. (j–l) OM pictures of hexagonal FeTe nanosheets with diverse thicknesses. (i and m) The stacked bar charts of the revolution of thickness with various growth time for tetragonal and hexagonal FeTe respectively. Scale bars: 20 μm in (b), (c) and (d); 10 μm in (f), (g), (h), (j), (k) and (l).

0.9 nm (~1 layers) shown in the atomic force microscopy (AFM) in Fig. S4. Similarly, by tuning the growth time, hexagonal FeTe crystals with various thicknesses are illustrated as Fig. 1g-l, respectively. As for the nonlayered hexagonal FeTe, the AFM images in Fig. S4 indicate that the thickness of the nanoplates can be controlled down to 2.3 nm. The statistical diagrams are displayed as Fig. 1i and 1 m. For these two kinds of FeTe, the thickness of the resulted samples increases with the deposition time. Even though the nanosheets with different thickness can be obtained at the same deposition time, the samples with a certain thickness still play a dominant role and the tendency indicates that the thickness increases with deposition time.

Spectral characterizations of different FeTe nanosheets

Raman spectroscopy is conducted to study the vibration of the chemical bonds from these two crystals. Fig. 2a displays the Raman spectra of tetragonal phase FeTe with various thicknesses, where two typical peaks at 158 cm^{-1} and 197 cm^{-1} can be indexed to the A_{1g} and B_{1g} mode, respectively, consistent with the previous report [48]. Notably, the intensity of B_{1g} gradually shrinks with reduced thickness, which may be caused by the oxidation and decomposition of thin FeTe crystals. With the thickness going down, the stability becomes worse, resulting in amorphous Te and TeO_2 covered on the surface of the samples to make the B_{1g} mode annihilate in thin layers [49]. Interestingly, only one peak

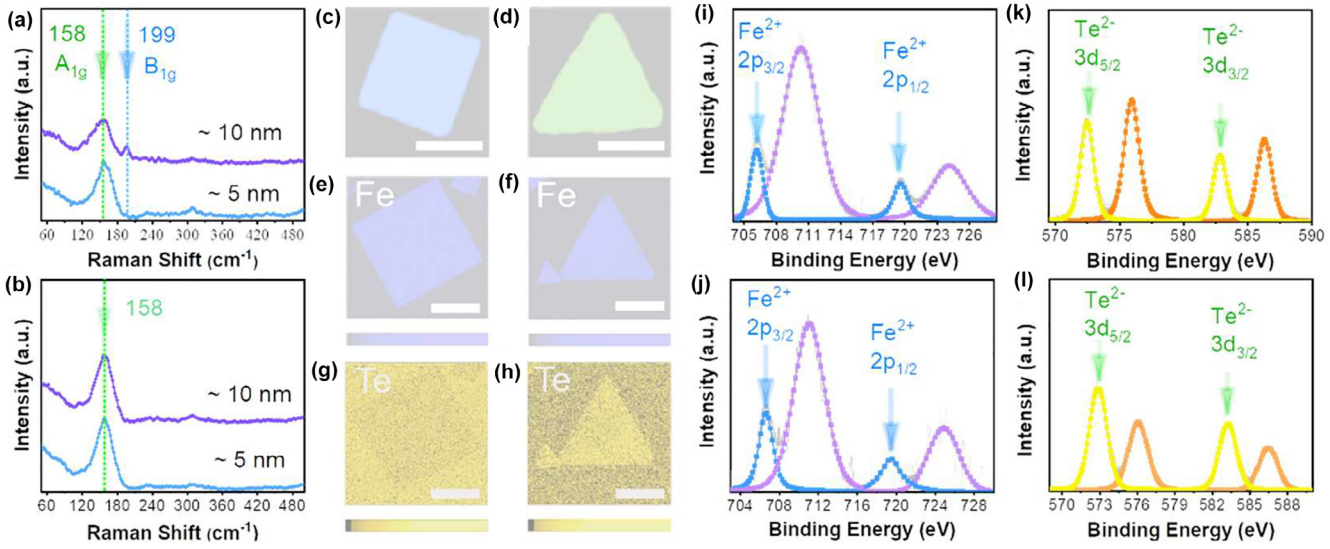

FIGURE 2

The characterizations of chemical bonds and states of FeTe crystals. (a, b) Raman spectra of square and hexagonal FeTe nanosheets with different thickness, respectively. (c, d) Raman mapping of tetragonal and hexagonal FeTe crystals. (e–h) Auger electron spectroscopy (AES) of tetragonal and hexagonal FeTe crystals, respectively. (i–l) X-ray photoemission spectroscopy (XPS) spectra of the Fe 2p and Te 3d from tetragonal and hexagonal FeTe nanosheets, respectively. Scale bars: 5 μm in (c) and (d); 2 μm in (e), (f), (g) and (h).

appears in the hexagonal phase FeTe located at 158 cm^{-1} similar to the A_{1g} in tetragonal phase FeTe in Fig. 2b. The slight difference between the Raman spectra of the tetragonal and hexagonal FeTe further confirms their different crystal structures. Raman mapping and AES mapping are carried to display the homogeneity of chemical distribution. Fig. 2c displays the B_{1g} mapping result of vibration mode in tetragonal FeTe while Fig. 2d shows the Raman mapping at 158 cm^{-1} in hexagonal FeTe crystals. The uniform color distribution in Fig. 2c-h indicates the elemental and chemical homogeneity in these two types of crystals.

The chemical states of the resulting FeTe samples are further analyzed by X-ray photoemission spectroscopy (XPS). Fig. 2i and 2j demonstrate the Fe 2p core-level spectrums of tetragonal and hexagonal FeTe crystal respectively. The blue peaks in Fig. 2i at 706.3 and 719.6 eV correspond to Fe^{2+} $2p_{3/2}$ and Fe^{2+} $2p_{1/2}$ of tetragonal FeTe while the two blue peaks of Fe^{2+} $2p_{3/2}$ and Fe^{2+} $2p_{1/2}$ for hexagonal FeTe is located at 706.6 and 719.4 eV [50]. The small difference of $Fe2p_{3/2}$ in these two FeTe crystals indicates the difference of the oxidation state in Fe, where Fe shows a higher oxidation state in hexagonal FeTe. The purple peaks at 710.2 and 710.8 eV in Fig. 2i and 2j stand for Fe^{3+} $2p_{3/2}$ together with 724.2 and 724.7 eV representing Fe^{3+} $_{1/2}$ respectively, which may come from the oxidation of the samples [51]. The yellow peak at 572.4 eV and 583.1 eV in Fig. 2k can be indexed to Te^{2-} $3d_{5/3}$ and Te^{2-} $3d_{5/3}$, respectively [52]. In contrast, the binding energy of these two peaks in tetragonal FeTe is lower than that in hexagonal FeTe. The orange peaks in both Fig. 2k and 2l can be classified into Te^{4+} signals which may be caused by the oxidation of the samples [53], consistent with the appearance of Fe^{3+} in Fig. 2i and 2j.

Structural differences between FeTe phases

Aberration-corrected scanning transmission electron microscopy-annular dark field (STEM-ADF) imaging and energy-dispersive spectroscopy (EDS) are further applied to analyze the microscopic structure and chemical composition of the resulting nanoplates. Fig. 3a and 3g display the typical HAADF images of tetragonal and hexagonal FeTe nanoplates, among which the brighter atoms stand for Te and darker atoms represent Fe according to their atomic number Z. The whole images display homogeneous atomic alignment and structure, indicating the high quality of the as-synthesized FeTe crystals. As for tetragonal FeTe nanosheets, the zoom of the HAADF image shown in Fig. 3b illustrates that each Fe atom is surrounded by four Te atoms and the distance of two adjacent Fe atoms can be indexed to (100) planes with the crystal parameter of 0.38 nm, consistent with the XRD data (PDF- # 07–0140). The crystal parameters of (200) and (020) can also be calculated from the SAED displayed in Fig. 3c. The top and side views of the layered tetragonal FeTe crystal structure are shown in Fig. 3d, where the blue and yellow atoms represent Fe and Te atom respectively. Fe and Te elemental distribution characterized by EDS mapping in Fig. 3e and 3f is homogenous throughout the entire crystal. Additionally, the content of Fe and Te in the crystal is approximately 1:1, close to the chemical stoichiometry of tetragonal FeTe.

The zoom-in image of Fig. 3g is displayed in Fig. 3h, where each Fe atom is surrounded by six Te atoms and the crystal reveals an in-plane six-fold symmetry. The adjacent Fe atom can be utilized to recognize the (1 0 0) plane of the crystal with the space parameter 0.34 nm. A similar result can also be obtained from the SAED in Fig. 3i. Fig. 3j indicates the top and side view of the hexagonal crystal structure, obviously displaying a nonlayered nature. It is worth to note that the element Fe EDS mapping of the hexagonal nanoplates displays an interesting difference in Fig. 3k, where the yellow dash-dot marks the boundary of the normal hexagonal part (the chemical stoichiometry of Fe:Te is ~1:1) and Fe-rich area (the ratio of Fe:Te is ~1.3:1). The dif-

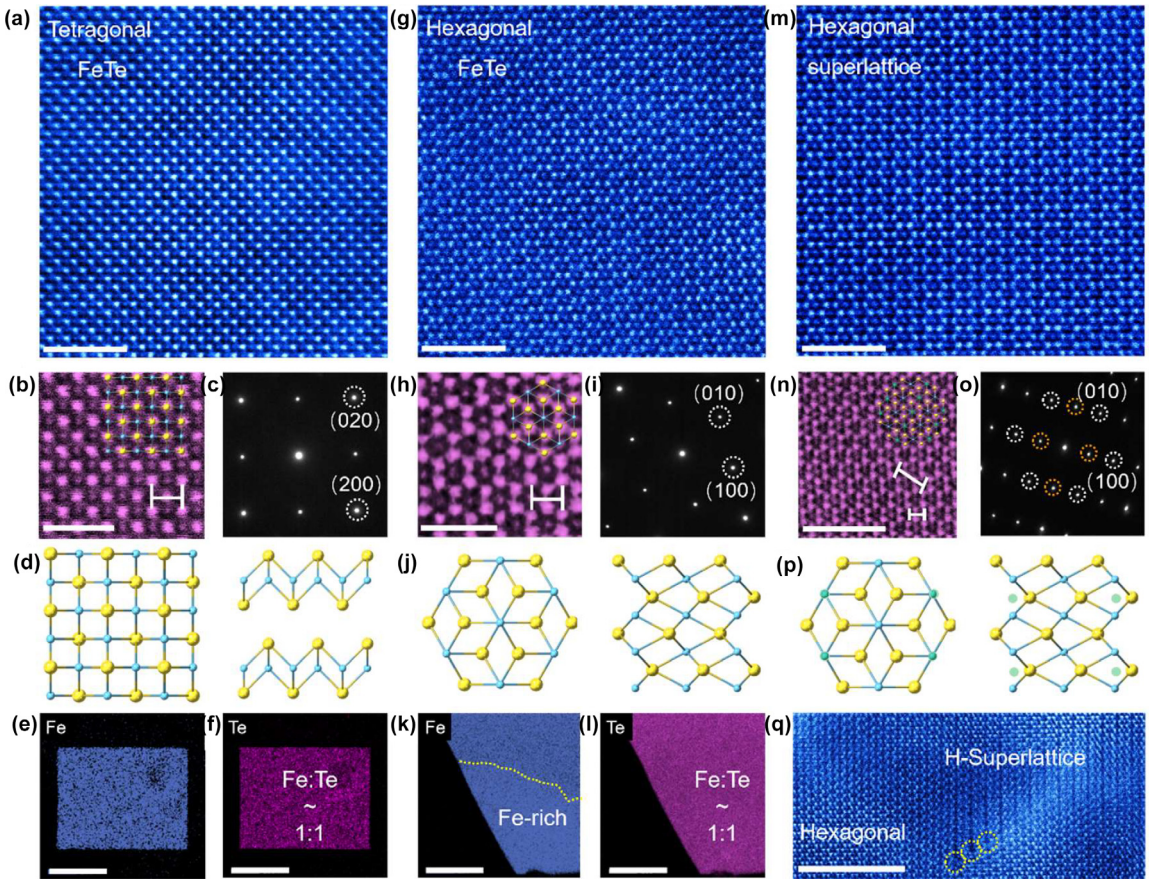

FIGURE 3

The crystal structures of different phase FeTe crystals from high-resolution transition electron microscopy. (a), (g), (m). High-angle annular dark-field scanning transmission electron microscopy images of tetragonal, hexagonal FeTe nanoplates, and hexagonal FeTe nanoplates with superlattice structure, respectively. (b, h, n) The magnificent high-angle annular dark-field (HAADF) images of the above images respectively. (c, i, o) The corresponding selected area electron diffraction (SAED) images. (d. j, p) The simulated crystal structure of tetragonal, hexagonal, and the superlattice FeTe. The left images represent the top view and the right one is side view, among which blue and yellow balls stand for iron and tellurium atom respectively. Besides, the green balls in p represent the anchored Fe atoms which may result in the superlattice structure. (e, f, k, l) The energy-dispersive spectroscopy (EDS) elemental analysis images of the square and hexagonal Fe nanoplates transferred on TEM grids respectively, where the yellow dotted line in k marks the boundary of normal hexagonal and superlattice area in the nanoplates. (q) The HAADF images of the boundary between the normal hexagonal and superlattice FeTe nanoplates. Scale bars: 2 nm in (a), (g), (m); 1 nm in (b) and (h) and (n); 5 nm in (q); 200 nm in (e) and (f); 400 nm in (k) and (l).

ference in Te element mapping is negligible compared to that in the Fe mapping.

To find out the reason of the difference of Fe distribution and probe the relationship between the composition and structure, HAADF analysis is conducted in the Fe-rich area as Fig. 3m shows. Obviously, the whole Fe-rich area illustrates a uniform superlattice structure showing the high quality of the hexagonal superlattice FeTe phase. Fig. 3n displays the zoom of the atomic alignment in hexagonal FeTe, where three kinds of atoms with different brightness mean different atom sites. The repeat unit of the superlattice can be measured as $0.71 \times 0.42\ nm^2$ while the simple hexagonal ring repeat unit is 0.36 nm, similar to that in Fig. 3h. The corresponding SAED results also display two sets of diffraction spots, consistent with Fig. 3n.

Therefore, given the fact that superlattice crystal owns a similar hexagonal ring structure with normal hexagonal FeTe crystals but indicates more Fe in the nanosheets, the possible crystal structure of the FeTe superlattice may be demonstrated as Fig. 3p. Extra Fe atom is arched between two adjacent Fe atoms causing the medium brightness atoms in HAADF, further resulting in the superlattice structure. Fig. 3q illustrates the boundary of the normal hexagonal crystal and superlattice crystal, where the upper part shows obvious superlattice structure. Notably, there are some point defects in the boundary marked in the yellow circles, which may be the reason to form a superlattice structure. More TEM images of FeTe samples with superlattice are shown in Figure S6 and S7.

Magneto-transport properties of FeTe nanosheets

Magneto-transport measurements are further performed to probe the magnetic and electrical properties of the as-grown tetragonal and hexagonal nanosheets (Fig. 4). Fig. 4a illustrates schematic diagrams of Hall-bar devices fabricated on tetragonal and hexagonal crystals, where Ti/Au metal stack is used as contact electrodes (see details in Methods). The magnetic field is applied perpendicularly to the nanosheets. Fig. 4b shows the temperature-dependent longitudinal resistance R_{xx} of a tetragonal FeTe nanosheet with thickness ~5 nm. The R_{xx} manifests rel-

atively small value (1084 Ω) at room temperature, indicating the possible metallic conduction. However, R_{xx} gradually increases followed by a sharp jump starting at 20 K as the temperature goes down, which differs significantly from typical metallic behaviors. For hexagonal FeTe, a ~4-nm-thick nanosheet in Fig. 4c shows different R_{xx}-temperature dependence compared with tetragonal nanocrystals show in Fig. 4b. The R_{xx} slowly increases with temperature decreasing from 300 to 30 K followed by a slight decreasing around 20 K and then rising again from 5 to 1.9 K.

Fig. 4d and 4e demonstrate the magnetoresistance (MR) of tetragonal and hexagonal FeTe crystals, respectively. In both phases, significant unsaturated linear magnetoresistance (LMR) can persist up to 9 T at low temperatures. The largest LMR 10.5% and 5.8% can be obtained at 1.9 K for tetragonal and hexagonal devices, respectively. The magnitudes of MR decrease with increasing temperature until it becomes negligible above 50 K.

The Hall resistances R_{xy} of tetragonal and hexagonal FeTe nanosheets at different temperatures are exhibited in Fig. 4f and 4g, respectively. All R_{xy} curves are linear with magnetic field representing a normal Hall effect, among which the negative and positive slopes indicate different carrier types in tetragonal and hexagonal FeTe nanosheets. No carrier type changing is observed in the measured temperature ranges for both phases.

Based on the MR and Hall measurements, no obvious hysteresis and anomaly have been observed for hexagonal crystal indicating no ferromagnetic ordering, which contrasts the recently published result [46] suggesting strong ferromagnetism in 4-nm hexagonal sample. The disappearance of ferromagnetic ordering in the hexagonal samples may result from the presence of degradation or disorders. Although great attention has been paid to preserve sample quality, including PMMA protective coating once samples are taken out of the furnace and device fabrication without intentional heating (see Methods for details), the extreme ambient sensitivity of FeTe nanosheets [46] may still result in a great amount of disorders and quench the magnetic ordering (Figure S11 show the degradation of FeTe in air). The presence of disorders creates spatial fluctuation and inhomogeneity in electrical conductivity, which can also explain the unsaturated LMR [54–57] observed in hexagonal as well as tetragonal nanosheets. As for the hexagonal FeTe with superlattice, detailed characterizations and device fabrication are hard to be

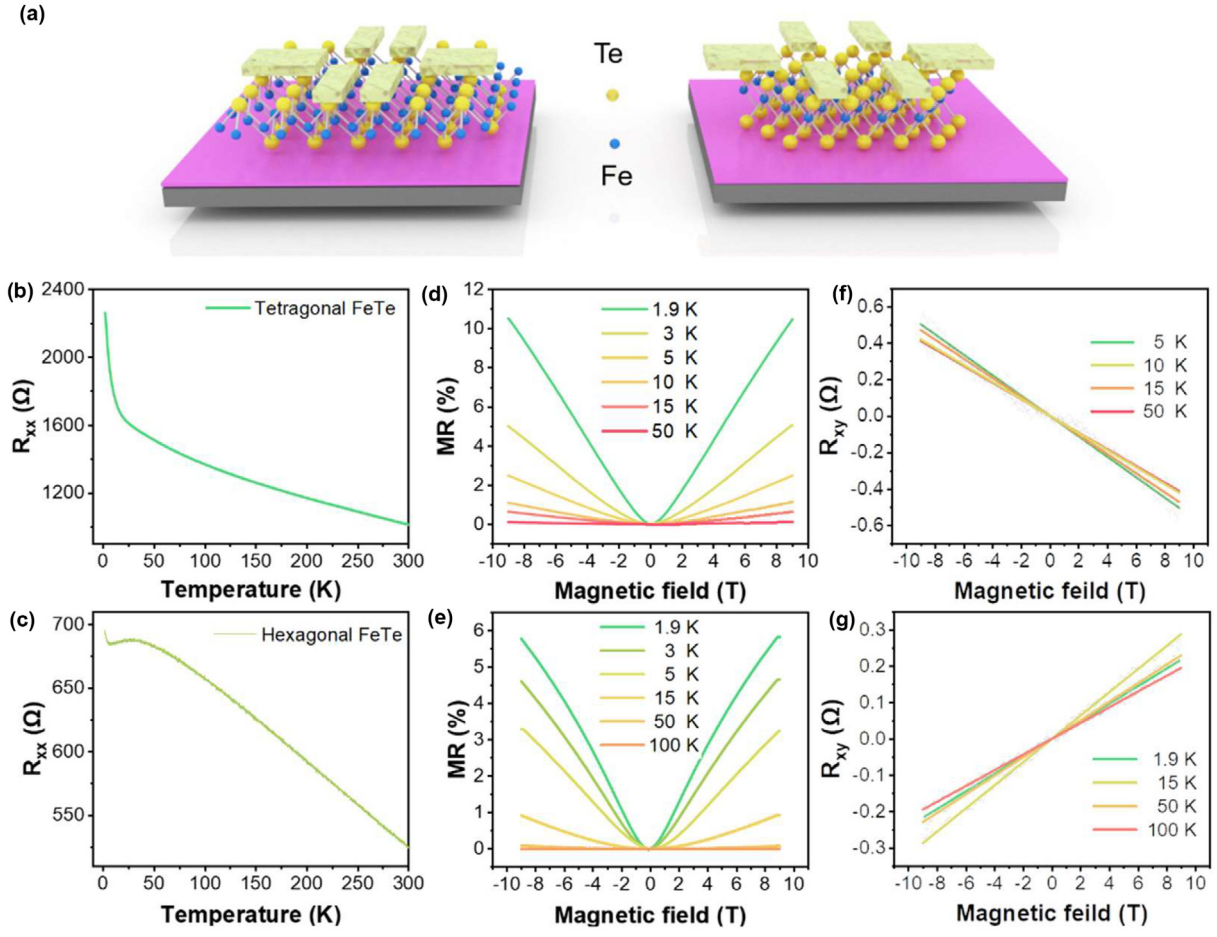

FIGURE 4

Magneto-transport properties of tetragonal and hexagonal FeTe nanosheets. (a) Illustrations of typical Hall-bar devices of individual tetragonal and hexagonal FeTe nanosheets on SiO_2/Si substrates, respectively. (b, c) Temperature dependence of resistance R_{xx} for tetragonal and hexagonal FeTe crystals from 300 to 1.9 K, respectively. (d, e) The revolutions of magnetoresistance, defined as $[R_{xx}(H)-R_{xx}(0)]/R_{xx}(0) \times 100\%$, of these two kinds of nanosheets characterized at different temperatures. (f, g) The magnetic field dependence of Hall resistance (R_{xy}) of these two kinds of nanosheets at different temperatures.

achieved because no effective methods except for TEM can help us to distinguish between normal and superlattice regions. Hence, more experiments should further be conducted to reveal the properties and potential applications of the hexagonal FeTe and its superlattice.

Emergence of superconductivity in oxygen-doped tetragonal FeTe nanosheets

Pristine tetragonal FeTe is a non-superconducting parent compound of Fe-based superconductors. However, the CVD-synthesized tetragonal FeTe nanosheet with thickness ~15 nm shown in Fig. 5a (Device 1 in Fig. S10) displays a sharp resistance drop around 9.0 K, indicating a possible superconducting transition. A similar sample, Device 2 in Fig. S10c, also shows the resistive transition, which further proves the emergence of superconductivity. Several routes can transform the tetragonal FeTe into a superconductor. First, substitutions of S or Se at Te sites introduce superconductivity by suppressing its antiferromagnetic ordering [58–61]. However, the quartz tube and corundum crucibles are used specific for CVD synthesis of FeTe such that the possibilities of S or Se contaminations can be eliminated. Also, it has been reported that superconductivity can be introduced into tetragonal FeTe thin films by tensile stress [62]. In contrast, the STEM and SAED in Fig. 3 agree well with the reported lattice constants, indicting no significant strain effects.

The observed superconductivity is strikingly robust to magnetic fields (persisting up to 16 T in Fig. 5b), suggesting its possible application as a supercurrent carrier under external field [63]. However, residual resistance appears in the superconducting tetragonal samples below their transition temperatures (see Device 2). The non-zero residual resistance may stem from the inhomogeneity of oxygen doping leaving non-superconducting patches inside the sample. More trivially, bad electrical contacts emitting Joule heat may locally destroy the superconductivity [65–69]. (SI shows the OM images of the devices)

These superconducting samples are bare against ambient without PMMA protection. It has been demonstrated that oxygen can be doped into FeTe thin films by exposure to ambient atmosphere even at room temperature. FeTe is then become a superconductor with doped oxygen [58,59,64,68]. Oxygen doping alters the Fe valency from Fe^{2+} in the non-superconducting state to mainly Fe^{3+} in superconducting state [64] as reproduced in the XPS measurement shown in Fig. 5d. Considering XPS is a surface-sensitive technique, AES depth analysis shown in Fig. 5e is further performed to reveal the presence of oxygen with concentration decreasing form surface to interior. Thick samples show better stability than ultrathin FeTe nanosheets, which causes more O concentration in thin FeTe than that in thick one as shown in Fig. 5e and 5f, respectively. Once the O concentration is beyond the moderate range, superconductivity will also vanish possibly due to over doping or structural degradation. Elemental analysis of micro-AES shows that O is enriched on the surface of a thick sample. The difference of the stability of thin and thick FeTe on the same substrate results in the different concentrations of O, which further leads to distinct electrical properties (no superconductivity is observed in the thin samples).

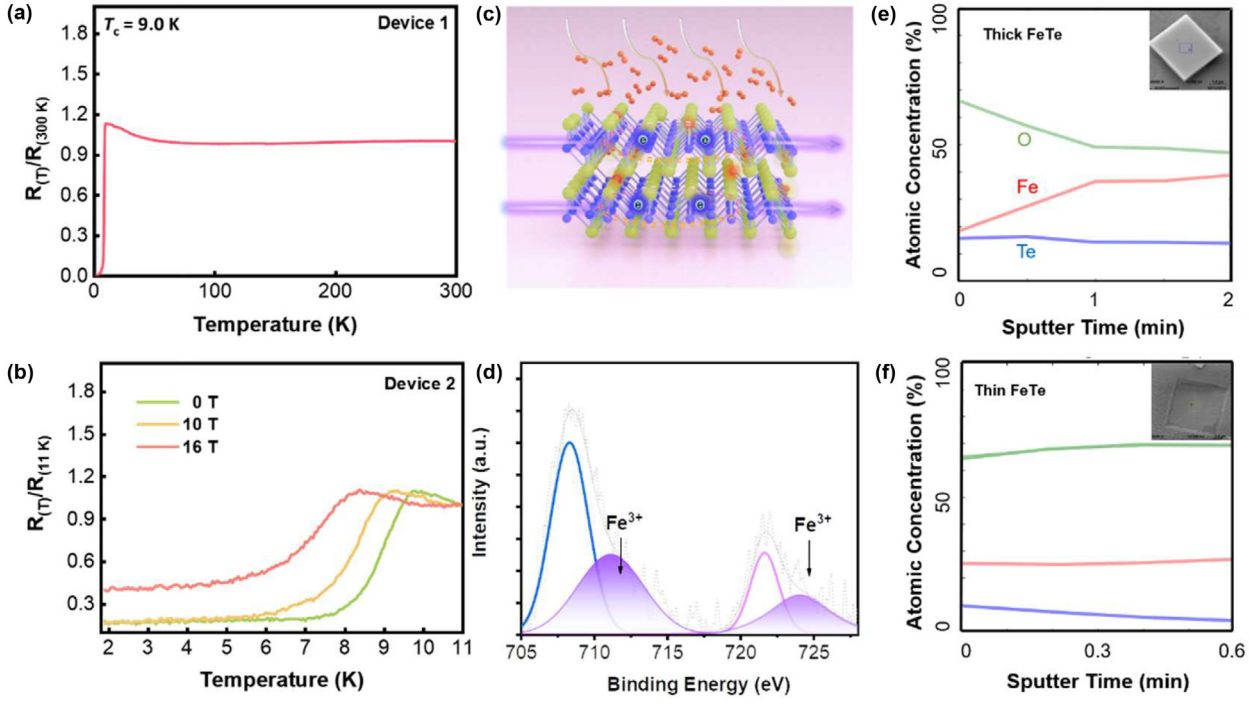

FIGURE 5

Superconducting behaviors of oxygen-doped tetragonal FeTe nanosheets. (a) The revolution of resistance with temperature, showing a superconducting transition at 9.0 K. (b) The superconductivity transition temperatures change with magnetic field. Interestingly, superconductivity can persist even at 16 T. (c) Illustration of the tetragonal FeTe doped by O atoms, where red, yellow, and blue balls represent O, Te, and Fe atoms respectively. (d) XPS results of the tetragonal FeTe. Purple peaks stand for the Fe^{3+} peak, which comes from the O doping. (e, f). Elemental depth analysis using AES of thick (15 nm) (with superconductivity) and thin (5 nm) tetragonal FeTe (without superconductivity). The sputtering rate is 3 nm/min.

Hence, we tentatively assign oxygen doping as the mechanism of superconductivity in the tetragonal FeTe nanosheets.

Conclusions

In conclusion, we utilize a facile chemical vapor deposition (CVD) approach to selectively synthesize ultrathin tetragonal (down to monolayer) and two kinds of hexagonal FeTe nanosheets by tuning the growth temperature according to the phase diagram. Magneto-transport measurements illustrate that the tetragonal crystals display a linear magnetoresistance (LMR) as high as 10.5% at 1.9 K and hexagonal nanosheets show 5.8% LMR at 1.9 K, indicating their potential applications as magnetoresistive devices. Meanwhile, tetragonal FeTe illustrates a superconducting transition at 9.0 K, which may be caused by oxygen doping. Notably, the Fe-rich hexagonal FeTe with superlattice offers an open and intriguingplatform to be further explored. In summary, this study illustrates a controllable way to selectively synthesize FeTe with different phases. Combined with the recent result on magnetic FeTe nanosheets [46], FeTe and its related compounds, including oxygen-doped FeTe, can serve as an intriguing material platfrom to explore 2D magnetism, supercondcutivity, and their heterostructures for potential applications in novel, functional devices.

Methods

Synthesis of FeTe nanosheets

CVD system was utilized to synthesize ultrathin FeTe nanosheets on SiO_2/Si substrates under atmospheric pressure. The thickness of thermally-oxidized SiO_2 layer is 285 nm. Ferrous chloride (0.1 g) (99.9%, Alfa) in a ceramic boat was placed in the center of the heating zone with a piece of SiO_2/Si substrate facing down above the powder. Tellurium powder (0.1 g) (99.999%, Acros) in a ceramic boat was placed in the upstream zone. Then ultrahigh purity argon (Ar) gas (~99.999%) was used to remove oxygen and moisture from the quartz tube. Afterward, the furnace was heated up to the target temperature from 600 to 750 °C in 18 min and held for several minutes from 1 to 10 min, together with the flow of mixed gases of 5 sccm H_2 and 45 sccm Ar. Once the reaction ends, the furnace was naturally cooled down to room temperature in the flow of 100 Ar. In order to preserve sample quality and reduce oxidation, samples were spin-coated with poly(methyl methacrylate) (PMMA, 950 A5) as soon as they were taken out of the tube. Note that samples with PMMA layers were then transferred into a vacuum desiccator overnight at room temperature without baking.

Sample characterizations

Optical microscope (CX44, OLYMPUS) and atomic force microscope (ICON, VEECO/BRUKER) were used to display the morphology and thickness of the as-grown FeTe nanosheets, respectively. The chemical composition, chemical states, and compositional homogeneity of the ultrathin nanosheets were determined by Raman spectra and mapping (DXRxi, Thermo) with a 532 nm laser as the excitation source, XPS (250Xi, Thermo Scientific Escalab) and AES mapping (PHI710, ULVAC-PHI). Aberration-corrected scanning transmission electron microscopy–annular dark field (ARM200F, JEOL) imaging and energy-dispersive spectroscopy (EDS) were further applied to analyze the microscopic structure and chemical composition of the resulting nanoplates.

Device fabrication and test

All Hall-bar devices were fabricated by a standard e-beam lithography process. 5 nm Ti and 60 nm Au were deposited sequentially as contact electrodes by e-beam evaporation. The magneto-transport measurements were performed in a Quantum Design Physical Property Measurement System (PPMS). An AC excitation current was applied between source and drain electrodes using a Keithley 6221 current source. The longitudinal and Hall voltages were then monitored by lock-in amplifiers (Stanford Research SR860).

Declaration of Competing Interest

The authors declare that they have no known competing financial interests or personal relationships that could have appeared to influence the work reported in this paper.

Acknowledgments

This work was supported by the National Key R&D Program of China (Grant No. 2018YFĂ900, 2016YFA0202300, 2018YFA0305800) and the Natural Science Foundation of China (51872012).

Contribution of authors

The project was supervised by **Yongji Gong; Xingguo Wang** and **Ce Bian** achieved the idea; **Anmin Nie** carried out the electron microscopy tests and image correlation analyses; **Ce Bian** and **Lihong Bao** performed the magneto-transport test and analysis; **Yixiang He** and **Jie Guo** helped to optimize the growth condition. XPS, AES and Raman tests were conducted and analyzed by **Peng Zhang, Lingjia Meng** and **Huaning Jiang** respectively; **Lixuan Liu** and **Bixuan Li** conducted SQUID test; **Yi Wei** was responsible for drawing growth schematics; **Xingguo Wang** wrote the original manuscript. All authors all contributed to the analysis and interpretation of the data and have opportunities to comment on the final version of the manuscript.

Data availability

The raw/processed data required to reproduce these findings cannot be shared at this time due to technical or time limitations.

Appendix A. Supplementary data

Supplementary data to this article can be found online at https://doi.org/10.1016/j.mattod.2020.11.022.

References

[1] Y. Cao et al., Nature 556 (2018) 43–50.
[2] Y. Yu et al., Nature 575 (2019) 156–163.
[3] M. Gibertini et al., Nat. Nanotechnol. 14 (2019) 408–419.
[4] C. Gong et al., Nature 546 (2017) 265–269.
[5] B. Huang et al., Nature 546 (2017) 270–273.
[6] D.J. Rizzo et al., Nature 560 (2018) 204–208.
[7] C. Cui et al., Nano Lett. 18 (2018) 1253–1258.
[8] Z.W. Li et al., Adv. Mater. 30 (2018) 1801908.
[9] S.D. Lei et al., Nano Lett. 15 (2015) 259–265.

[10] X. Zhang et al., Nature 566 (2019) 368–372.
[11] Y. Gong et al., Nat. Nanotechnol. 4 (2018) 294–1288.
[12] C. Jiang et al., Nat. Commun. 9 (2018) 753.
[13] S. Shamoto et al., Physica C. 306 (1998) 7–14.
[14] C. Felser et al., J. Mater. Chem. 9 (1999) 459–464.
[15] H. Wang et al., Nat. Commun. 8 (2017) 394.
[16] H. Lian et al., Physica C. 538 (2017) 27–31.
[17] Y. Hamaue et al., J. Phys. Soc. Jpn. 55 (1986) 1327–1335.
[18] R. Zhang et al., Nano Lett. 16 (2016) 629–636.
[19] J.H. Tapp et al., Phys. Rev. B 78 (2008) 060505.
[20] D. Liu et al., Nat. Commun. 3 (2012) 931.
[21] Y. Mizuguchi et al., J. Phys. Soc. Jpn. 78 (2009) 074712.
[22] C. Xu et al., Nat. Mater. 14 (2015) 1135–1141.
[23] Z. Fei et al., Nat. Mater. 17 (2018) 778–782.
[24] N. Wang et al., J. Am. Chem. Soc. 141 (2019) 17166–17173.
[25] J. Liu et al., Phys. Chem. Chem. Phys. 18 (2016) 8777–8784.
[26] J. Li et al., Adv. Mater. 30 (2018) 1801043.
[27] F. Cui et al., Adv. Mater. 32 (2020) 1905896.
[28] J. Yuan et al., Nano Lett. 19 (2019) 3777–3781.
[29] H. Duan et al., Nat. Commun. 10 (2019) 1584.
[30] T. Song et al., Nat. Mater. (2019) 1–5.
[31] T. Li et al., Nat. Mater. 18 (2019) 1303–1308.
[32] M. Monni et al., Phys. Rev. B 87 (2013) 094516.
[33] Y. Deng et al., Nature 563 (2018) 94–99.
[34] N. Mounet et al., Nat. Nanotechnol. 13 (2018) 246–252.
[35] H. Lv et al., Phys. Rev. B 92 (2015) 214419.
[36] A. Subedi et al., Phys. Rev. B 78 (2008) 134514.
[37] M. Kan et al., Phys. Chem. Chem. Phys. 16 (2014) 4990–4994.
[38] O.K. Von Goldbeck, IRON—Binary Phase Diagrams, Springer, 1982.
[39] S. Chen et al., ACS Nano 14 (2020) 11473–11481.
[40] G. Grechnev et al., J. Phys.: Condens. Matter 26 (2014) 436003.
[41] A. Sklyarova et al., J. Magn. Magn. Mater. 329 (2013) 129–132.
[42] P. Maheshwari et al., Mater. Res. Express 5 (2018) 126002.
[43] T. Taen et al., Phys. Rev. B 80 (2009) 092502.
[44] L. Narangammana et al., Appl. Phys. Lett. 103 (2013) 102604.
[45] D.S.J.S.R. Parker, Sci. Rep. 7 (2017) 1–6.
[46] L. Kang et al., Nat. Commun. 11 (2020) 3729.
[47] K.D. Oyler et al., Chem. Mater. 21 (2009) 3655–3661.
[48] T.-L. Xia et al., Phys. Rev. B 79 (2009) 140510.
[49] A. Pine, G.J.P.R.B. Dresselhaus, Phys. Rev. B 4 (1971) 356.
[50] K. Laajalehto et al., Appl. Surf. Sci. 81 (1994) 11–15.
[51] J. Langevoort et al., Appl. Surf. Sci. 28 (1987) 167–179.
[52] L. Soriano et al., Surf. Interface Anal. 16 (1990) 193–198.
[53] X. Chia et al., Chem. - Eur. J. 23 (2017) 11719–11726.
[54] A.A. Abrikosov, Phys. Rev. B 58 (1998) 2788–2794.
[55] J. Hu, T.F. Rosenbaum, Nat. Mater. 7 (2008) 697–700.
[56] H. Chen et al., J. Am. Chem. Soc. 141 (2018) 635–642.
[57] M. Parish et al., Nature 426 (2003) 162–165.
[58] Y. Nie et al., Phys. Rev. B 82 (2010) 020508.
[59] W. Si et al., Phys. Rev. B 81 (2010) 092506.
[60] B.C. Sales et al., Phys. Rev. B 79 (2009) 094521.
[61] Y. Mizuguchi et al., Appl. Phys. Lett. 94 (2009) 012503.
[62] Y. Han et al., Phys. Rev. Lett. 104 (2010) 017003.
[63] N.E. Litombe et al., Phys. C 506 (2014) 169–173.
[64] Zheng, M., et al., arXiv preprint arXiv:1301.4696 (2013).
[65] C. Benvenuti et al., Physica C 316 (1999) 153–188.
[66] J. Li et al., Nat. Commun. 6 (2015) 7614.
[67] B.I. Halperin et al., Resistance in superconductors, in: Bcs: 50 Years, World Scientific, 2011, pp. 185–226.
[68] H. Hu et al., Phys. Rev. B 90 (2014) 180504.
[69] J. Wang et al., Phys. Rev. B 86 (2012) 035439.